crystals

MDPI

Article

Optical Photon Propagation Characteristics and Thickness Optimization of $LaCl_3$:Ce and $LaBr_3$:Ce Crystal Scintillators for Nuclear Medicine Imaging

Stavros Tseremoglou [1], Christos Michail [1], Ioannis Valais [1], Konstantinos Ninos [2], Athanasios Bakas [2], Ioannis Kandarakis [1], George Fountos [1] and Nektarios Kalyvas [1,*]

[1] Radiation Physics, Materials Technology and Biomedical Imaging Laboratory, Department of Biomedical Engineering, University of West Attica, Ag. Spyridonos, 12210 Athens, Greece
[2] Department of Biomedical Sciences, University of West Attica, Ag. Spyridonos, 12210 Athens, Greece
* Correspondence: nkalyvas@uniwa.gr; Tel.: +30-210-5385319

Abstract: The present study focuses on the determination of the optimal crystal thickness of $LaCl_3$:Ce and $LaBr_3$:Ce crystal scintillators for Nuclear Medicine Imaging applications. A theoretical model was applied for the estimation of the optical efficiency of the two single-crystal scintillators in terms of Detector Optical Gain (*DOG*). The theoretical model was validated against the experimental values of the Absolute Efficiency (*AE*) of the two crystals, obtained in the energy range 110 kVp–140 kVp. By fitting the theoretical model to these experimental data, the propagation probability per elementary thickness k was determined and *DOG* was theoretically calculated for crystal thicknesses from 0.005 cm to 2 cm, in the energy range of Nuclear Medicine Imaging. k values for $LaCl_3$:Ce and $LaBr_3$:Ce crystals were significantly higher compared to other single-crystal scintillators. The *DOG* values of the two crystals may serve as evidence that the $LaBr_3$:Ce crystal exhibits significantly better performance compared to the $LaCl_3$:Ce crystal. With an increase in energy, the optimum thickness increases for both crystals. Additionally, crystal efficiency generally demonstrates a decrease beyond a certain thickness. The aforementioned insights may provide valuable guidance for the design and optimization of crystal scintillators in Nuclear Medicine Imaging systems.

Keywords: $LaBr_3$:Ce; $LaCl_3$:Ce; modeling; Nuclear Medicine Imaging applications

Citation: Tseremoglou, S.; Michail, C.; Valais, I.; Ninos, K.; Bakas, A.; Kandarakis, I.; Fountos, G.; Kalyvas, N. Optical Photon Propagation Characteristics and Thickness Optimization of $LaCl_3$:Ce and $LaBr_3$:Ce Crystal Scintillators for Nuclear Medicine Imaging. *Crystals* **2024**, *14*, 24. https://doi.org/10.3390/cryst14010024

Academic Editor: Yutaka Fujimoto

Received: 4 December 2023
Revised: 18 December 2023
Accepted: 25 December 2023
Published: 26 December 2023

1. Introduction

Nuclear Medicine Imaging provides functional or metabolic information by imaging the distribution and concentration of a radiolabeled compound within the body. There are two main modalities in Nuclear Medicine Imaging, single photon imaging, which includes conventional (planar) scintigraphy along with single photon emission computed tomography (SPECT) and positron emission tomography (PET) [1]. The radionuclides used in single photon imaging are gamma emitters in the energy range from about 60 keV to 400 keV [1–3]. Such radioisotopes, as shown in Table 1, are ^{123}I, ^{201}Th, ^{67}Ga, ^{111}In, ^{131}I, and ^{99m}Tc, the latter being the most frequently utilized due to its numerous advantages [1–4].

Table 1. Nuclear Medicine radionuclides and their corresponding energies [2,4].

Radionuclides	γ Energy (keV) and % Ratio
^{123}I	159 (83%)
^{201}Tl	71 (47%), 80 (20%), 167 (10%)
^{67}Ga	93 (40%), 185 (20%), 300 (17%), 393 (20%)
^{111}In	171 (90%), 245 (94%)
^{131}I	365 (82%)
^{99m}Tc	140 (89%)

The radioisotopes used in PET emit β^+ particles which interact with electrons inside the patient's body and then annihilate, producing two photons, each with an energy of 511 keV. [1]. Nowadays, SPECT and PET are combined with X-ray Computed Tomography (CT) in hybrid systems SPECT/CT and PET/CT. These systems, through the combination of anatomical and functional information, obtained in the same imaging session very close together in time, and the improvement in attenuation correction, provide the opportunity for a more accurate diagnosis [1,5–12]. The efficiency of these hybrid systems could be further improved if a common detector was utilized to operate both modalities [13,14].

Two scintillators that are potential candidates for that common detector unit, owing to their appealing characteristics, are $LaCl_3$:Ce and $LaBr_3$:Ce crystals. These crystals have a large light yield, 49,000 photons/MeV and 63,000 photons/MeV, fast response with decay times 28 ns and 25 ns, excellent energy resolution, 3.8% and 2.6%, and max wavelength emission at 350 and 380 nm, respectively [15–20]. In Table 2, some of the properties of the two crystals are presented. Their suitability for hybrid imaging systems has already been investigated under X-ray excitation in previous studies [21,22].

Table 2. $LaCl_3$:Ce and $LaBr_3$:Ce crystal properties [19,20].

Properties	$LaCl_3$:Ce	$LaBr_3$:Ce
Wavelength, max emission (nm)	350	380
Decay Time (ns)	28	25
Light Yield (photons/MeV)	49,000	63,000
Radiation Length (cm)	2.813	1.881
Density (g/cm^3)	3.86	5.2
Hardness (Mho)	3	3
Reflection Loss/Surface (%)	6.8	6.8
Lattice constant (nm)	0.6196	0.6196

Due to their exceptional performance in brightness and response time, these crystals continue to be subjects of investigation and comparison with other crystals already in use [23–26]. Apart from medical imaging, their use has been explored in the detection of protons in nuclear reactions [27], simultaneous detection of high-energy protons and gamma rays in nuclear reactions, as well as in the precise determination of the radioactive dose in carbon ion therapy, and in proton tomography [28]. Furthermore, their use has been examined in innovative gamma-ray detection systems with position sensitivity [29], in a common detector for neutrons and gamma rays [30], in the detection of gamma rays in a nuclear power reactor [31], and in the application for a Compton camera used in proton beam monitoring in hadron therapy [32].

The optical performance of the detector is greatly influenced by the thickness of the scintillation crystal when considering a specific X-ray or gamma-ray energy spectrum. In particular, the thickness of the crystal affects the detection efficiency and the intrinsic spatial resolution [1]. In addition, an optimal thickness can lead to the production of a high-intensity signal, thus reducing the amount of radiopharmaceutical required to be injected into the patient, leading to faster imaging and a lower patient dose. The present study focuses on the determination of the optimal crystal thickness of the aforementioned crystals for Nuclear Medicine Imaging applications. For this purpose, a theoretical model [33–36] is applied for the estimation of the optical efficiency of the two single-crystal scintillators in terms of Detector Optical Gain (*DOG*), i.e., the number of emitted optical photons per incident X- or gamma-ray photons [33,35]. The model describes the light collection efficiency of a single crystal as a function of thickness and incident X-ray or gamma-ray energy.

The theoretical model was validated against the experimental values of the Absolute Efficiency (*AE*) of the two crystals, i.e., the ratio of the energy flux of light emitted by the crystal to the rate of incident X-ray exposure [21,22]. The propagation probability per elementary thickness k was used to theoretically calculate *DOG* for crystal thicknesses

from 0.005 cm to 2 cm, in the energies corresponding to Nuclear Medicine Imaging utilized radiopharmaceuticals. The optimum scintillator thickness determined for both generic (i.e., bone imaging, kidney imaging) or more specific (i.e., thyroid, heart) examinations, as well as for PET applications, may lead to a design of Nuclear Medicine Imaging instrumentation based on $LaCl_3$:Ce and $LaBr_3$:Ce scintillators, with increased examination speed and radiation dose savings to the patient.

2. Materials and Methods

According to the applied theoretical model, the crystal can be divided into N elementary layers. Only a percentage, hereafter called k, of the photons generated in the n^{th} layer passes to the $n + 1$ layer and from there to the next, eventually reaching the output surface of the crystal. The model assumes that this percentage k remains constant for each layer. The loss of optical photon energy in the crystal is assumed to occur either by internal optical photon absorption in the crystal mass or by optical photon escape when the photons reach the crystal surfaces. The model also considers the X-ray attenuation properties in the crystal, the intrinsic conversion efficiency, showing the fraction of the absorbed X-ray or gamma-ray energy converted into optical photon energy [36], and the reflection of the optical photons at the input and output crystal surfaces. A more in-depth explanation of the model has been described in previous studies [33,35].

It is hypothesized that an equal number of optical photons, produced within the crystal's mass, are traveling in both forward and backward directions [33,35]. By considering all the reflections that occur between the entrance and the exit surfaces of the scintillator, we can determine the proportion of optical photons, produced in the nth layer, that manage to escape the crystal by the relation [35]:

$$M_n = (1 - R_0)\left[\frac{k^{N-n}}{1 - k^{2N} R_0\, R_1} + R_1 k^{n+N} \frac{k^{2N} R_0 R_1}{1 - k^{2N} R_0 R_1}\right] \quad (1)$$

where R_0 is the output reflectivity, denoting the fraction of photons reflected back into the scintillator when incident at its exit surface, and R_1 is the input reflectivity, referring to the proportion of optical photons that are reflected back into the scintillator upon encountering its entrance surface. Both cubic crystals are wrapped with Teflon tape on their five surfaces, resulting in a high reflectivity close to 100% (R_1 = 1) for these surfaces [37]. The exit surface of the crystals in contact with the photodetector is protected with silicon glass. Consequently, when determining the R_0, the reflection coefficients of crystal–silicon glass interface ($R_{cr,Si}$) and silicon glass–air interface ($R_{Si,air}$) were taken into consideration. A fraction ($1 - R_{cr,Si}$) of the incident light on the exit surface of the crystal passes through the interface between the crystal and silicon glass. Subsequently, this fraction reaches the interface between glass and air, where a fraction $R_{Si,air}$ of it, is reflected and directed back towards the crystal. In this approach, an error of approximately 1.5% arises due to reflections on the crystal–glass interface. Considering the above, R_0 is given by the following relation:

$$R_0 = (1 - R_{cr,Si})\, R_{Si,air} \quad (2)$$

$R_{cr,Si}$ and $R_{Si,air}$ are defined as [33]:

$$R_{cr,Si} = \frac{(n_1 - n_2)^2}{(n_1 + n_2)^2} \quad (3)$$

and

$$R_{Si,air} = \frac{(n_2 - 1)^2}{(n_2 + 1)^2} \quad (4)$$

The refractive indexes n_1 = 1.9 of the crystals and n_2 = 1.47 of the silicon glass used in relations (3) and (4) were obtained from the literature [38–40].

Considering all of the layers, the total amount of optical photons generated by X-rays with energy E and manage to exit through the output is equal to [35,36]:

$$M(E) = \sum_{n=1}^{N} f(E) e^{-\mu_{Al} t} e^{-\mu n \Delta t} \mu \Delta t n_c \frac{E}{E_\lambda} (1 - R_0) \left[\frac{k^{N-n}}{1 - k^{2N} R_0 R_1} + R_1 k^{n+N} \frac{k^{2N} R_0 R_1}{1 - k^{2N} R_0 R_1} \right] \quad (5)$$

where *f(E)* is the incident X-ray fluence obtained from the TASMIP Spectra Calculator [41], μ is the attenuation coefficient, Δt is the thickness of each layer n of the scintillator, E_λ is the energy of the optical photons, and μ_{Al} and t are the attenuation coefficient and the thickness of the aluminum encapsulation of the crystal, respectively. n_c is the intrinsic conversion efficiency and it was calculated for a light yield of LY = 49.000 photons/MeV and LY = 63.000 photons/MeV for $LaCl_3$:Ce and $LaBr_3$:Ce crystals, respectively, by the relation [34,36]:

$$n_C = \frac{LY(E_\lambda)}{10^6} \quad (6)$$

The theoretical value of AE for a photon of specific energy is given by the following relation [33,34]:

$$AE(E) = \sum_{n=1}^{N} \gamma(E) e^{-\mu_{Al} t} e^{-\mu n \Delta t} \mu \Delta t n_c (1 - R_0) \left[\frac{k^{N-n}}{1 - k^{2N} R_0 R_1} + R_1 k^{n+N} \frac{k^{2N} R_0 R_1}{1 - k^{2N} R_0 R_1} \right] \quad (7)$$

where $\gamma(E)$ is a conversion factor converting energy fluence (W/m^2) into exposure rate (mR/s). Considering the whole energy spectrum, AE equals to [34]:

$$AE = \frac{\sum_{E=E_{min}}^{E_{max}} f(E) AE(E)}{\sum_{E=E_{min}}^{E_{max}} f(E)} \quad (8)$$

The propagation probability per elementary thickness k was determined from relation (8) by fitting the theoretical equation to experimental $AE(E)$ data. During the fitting procedure, different values of k were tested in Equation (8) and compared with the corresponding experimental AE results calculated. Different k values were tested arbitrarily (trial and error method). The final selected k value was the one where the results of Equation (8) were equal to the corresponding experimental AE data. These experimental data were obtained from crystals samples with 10 mm thicknesses, that are commonly used in CT applications (110 kVp–140 kVp) [21,22]. X-ray irradiation of the crystal samples was performed using an X-ray tube equipped with a 1.5 mm Al filter, connected to a CPI series CMP 200DR 50kW generator while maintaining a constant current-time product of 63 mAs and an irradiation duration of 1 s. Additionally, a 20mm Al filtration was introduced at the exit of the X-ray tube. The exposure rate was measured with RTI Piranha P100B dosimeter. The experimental setup for the energy flux measurement comprised a light integration sphere (Oriel 70451) coupled to a photomultiplier tube (PMT) (EMI 9798B) which was connected to an electrometer (Cary 400) [21,22].

Similarly, the DOG can be determined across the entire range of X-ray energy by the relation [35,36]:

$$DOG = \frac{\sum_{E=E_{min}}^{E_{max}} M(E)}{\sum_{E=E_{min}}^{E_{max}} f(E) e^{-\mu_{Al} t}} \quad (9)$$

For the calculation of DOG for radioisotopes, assuming that f_i is the probability of energy emission E_i, which has an attenuation coefficient μ_i, relation (5) transforms into the following form:

$$M_i(E_i) = \sum_{n=1}^{N} e^{-\mu_{Al} t} e^{-\mu_i \Delta t} \mu_i \Delta t n_c \frac{1}{E_\lambda} (1 - R_0) \left[\frac{k^{N-n}}{1 - k^{2N} R_0 R_1} + R_1 k^{n+N} \frac{k^{2N} R_0 R_1}{1 - k^{2N} R_0 R_1} \right] \quad (10)$$

Finally, the *DOG* was calculated as:

$$DOG = \frac{\sum_i f_i E_i M_i}{\sum_i f_i} \quad (11)$$

3. Results

Figure 1 displays the values of parameter *k* for $LaCl_3$:Ce and $LaBr_3$:Ce crystals within the tube voltage range of 110 kVp to 140 kVp, demonstrating the propagation of optical photons through each layer of 5 μm thickness. Both crystals present a stable performance, with the k values remaining almost constant (from 0.99776 to 0.99768 for $LaCl_3$:Ce and from 0.99876 to 0.99872 for $LaBr_3$:Ce). The results obtained for both crystals can be considered adequate, as the values of *k* remain above 0.99 over the entire range of voltages investigated.

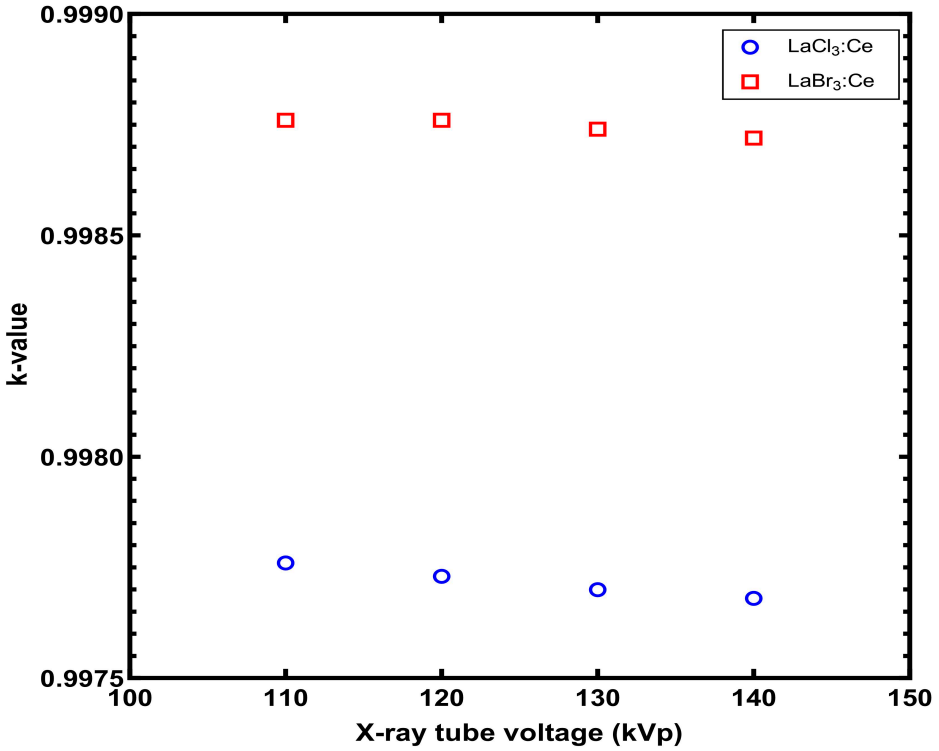

Figure 1. *k* values of $LaCl_3$:Ce and $LaBr_3$:Ce single crystals in X-ray tube voltage range of 110 to 140 kVp.

The data presented in Figures 2 and 3 allow for a comparison between the experimental [21,22] and theoretical values of *AE* for the two crystals. As shown in these figures, a strong agreement exists between the experimental observations and the theoretical predictions of *AE*, for both crystals. For the $LaCl_3$:Ce crystal, the relative difference between the experimental and the theoretical AE is between 0.05% and 3.86%. On the contrary, for the $LaBr_3$:Ce crystal, the relative difference between the experimental and the theoretical values ranges from 0.03% to 2.57%.

The theoretical *AE* values for $LaCl_3$:Ce and $LaBr_3$:Ce crystals were determined using an average k value of 0.9977 and 0.9987, respectively. For other scintillators, the values of the k coefficient, which were calculated using the same model and for an elementary layer thickness of 1 μm, range between 0.74 and 0.994. Specifically, for the single-crystal scintillators GSO:Ce, LSO:Ce, LYSO:Ce, and YAP:Ce, the corresponding *k* values were 0.923, 0.845, 0.860, and 0.74, respectively [33,36]. In the case of CsI:Tl columnar phosphor, the *k* value ranged from 0.980 to 0.994 for different column thicknesses [35].

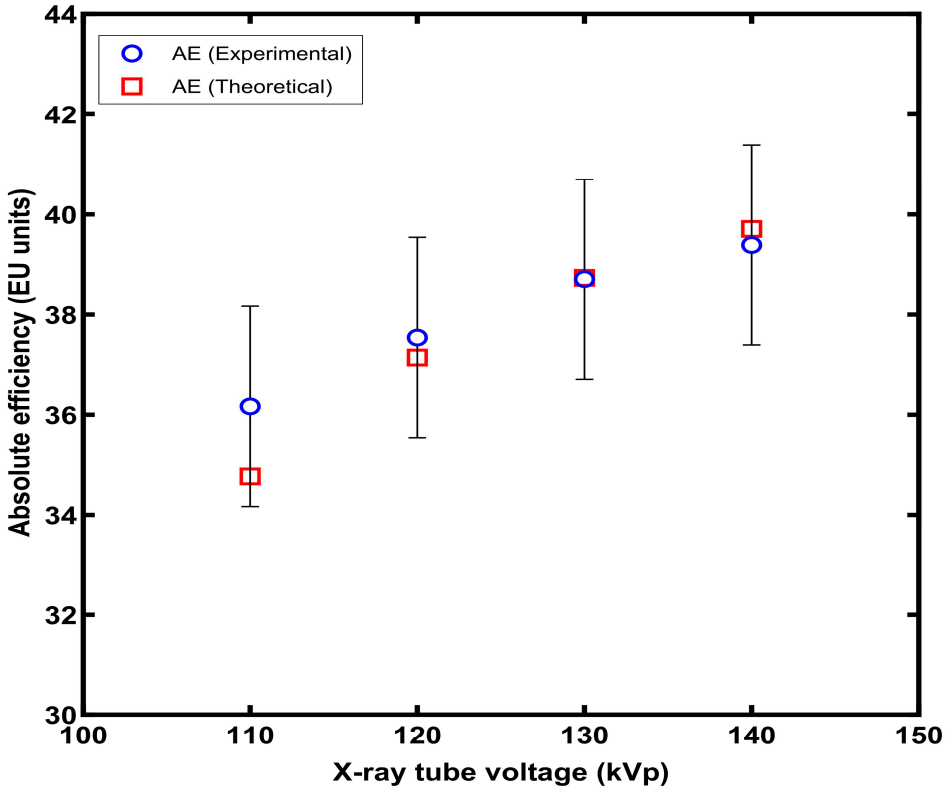

Figure 2. Theoretical and experimental *AE* (5.3% error bar) results for $LaCl_3$:Ce crystal.

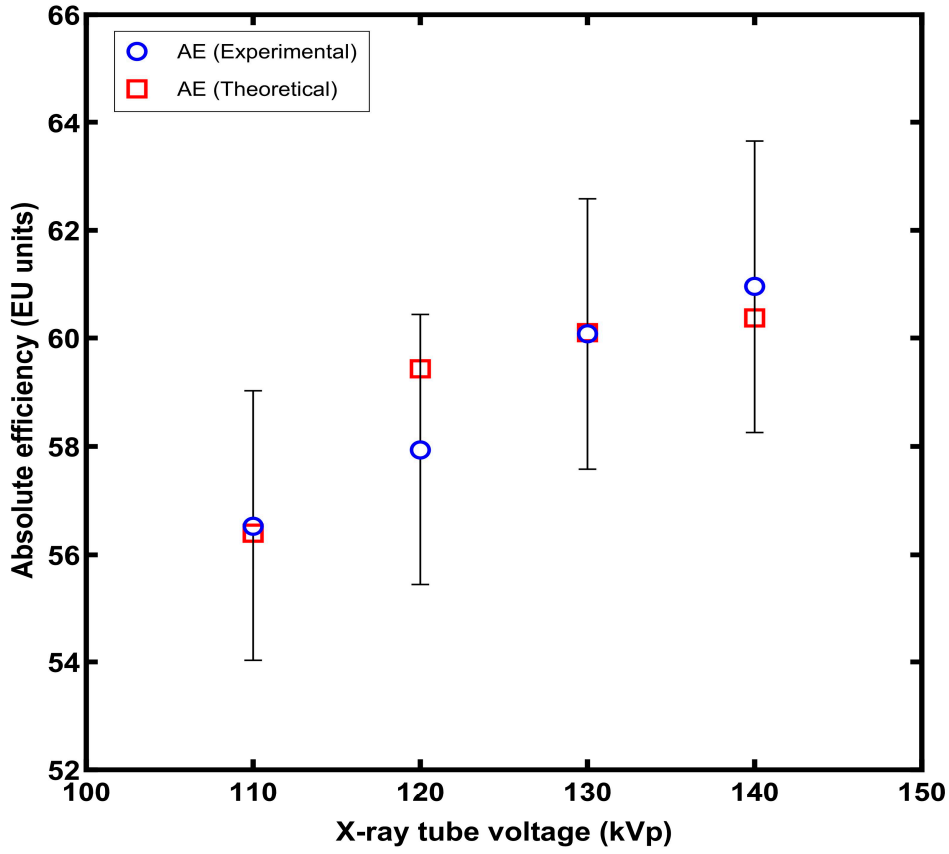

Figure 3. Theoretical and experimental *AE* (4.25% error bar) results for $LaBr_3$:Ce crystal.

Figures 4–8 present the *DOG* values that have been predicted for crystal thicknesses ranging from 0.005 cm to 2 cm, corresponding to various radioisotopes and X-ray energies. The results indicate that *DOG* values attributed to the $LaBr_3$:Ce crystal are generally higher than those of the $LaCl_3$:Ce crystal for all radioisotopes and X-ray energies examined. Another deduction derived from the findings is that the crystal efficiency demonstrates a decrease beyond a certain thickness. This is because although a higher crystal thickness enhances energy absorption, it also leads to increased loss of optical photons during propagation towards the output.

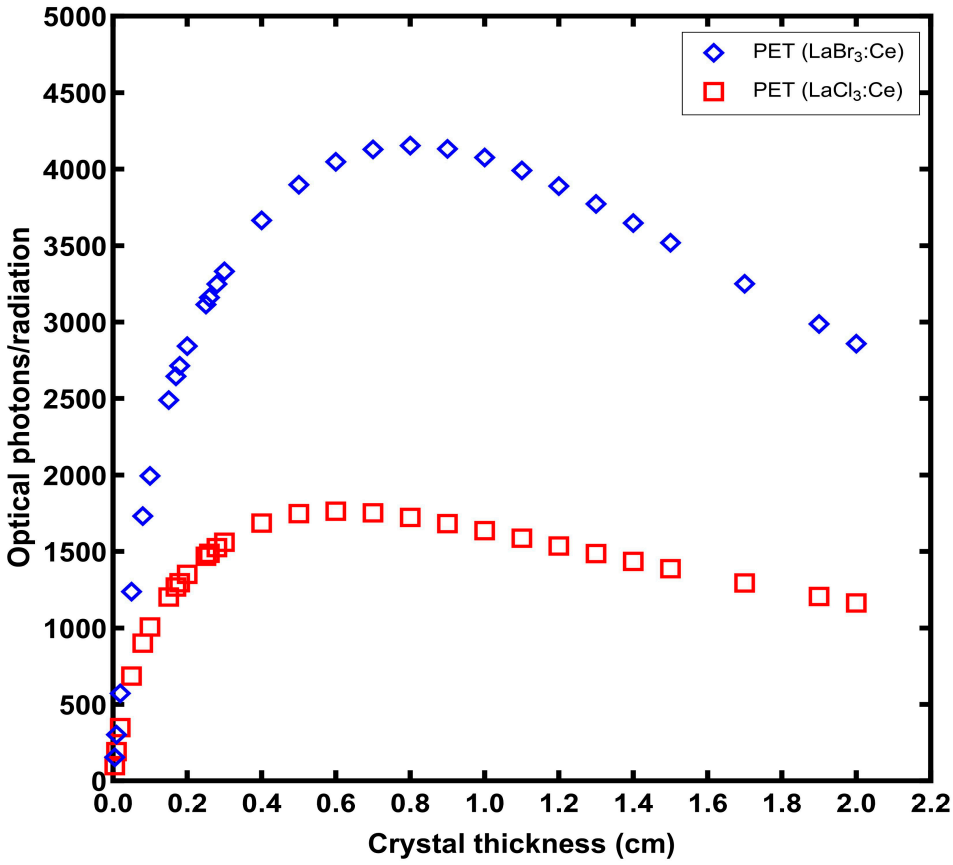

Figure 4. The predicted *DOG* values of $LaCl_3$:Ce and $LaBr_3$:Ce crystals for various thicknesses for 511 keV.

For various medical applications, different optimal crystal thicknesses have been identified for $LaCl_3$:Ce and $LaBr_3$:Ce crystals. Specifically, for PET applications, the $LaCl_3$:Ce crystal demonstrates optimal performance with a thickness of 0.6 cm, whereas the $LaBr_3$:Ce crystal performs best at 0.8 cm. Both crystals, however, show ideal thicknesses of 0.3 cm and 0.1 cm for ^{99m}Tc and ^{201}Tl applications, respectively. For ^{131}I applications, the optimal thickness is 0.5 cm for $LaCl_3$:Ce and 0.7 cm for $LaBr_3$:Ce, whereas for ^{123}I applications, both crystals exhibit an ideal thickness of 0.3 cm. Additionally, both crystals demonstrate ideal performance for ^{111}In and ^{67}Ga applications with a thickness of 0.4 cm. Moreover, for X-ray energies of 120 kVp and 140 kVp, the $LaCl_3$:Ce crystal shows optimal thickness at 0.2 cm, whereas the $LaBr_3$:Ce crystal exhibits the best performance at 0.08 cm and 0.1 cm, respectively.

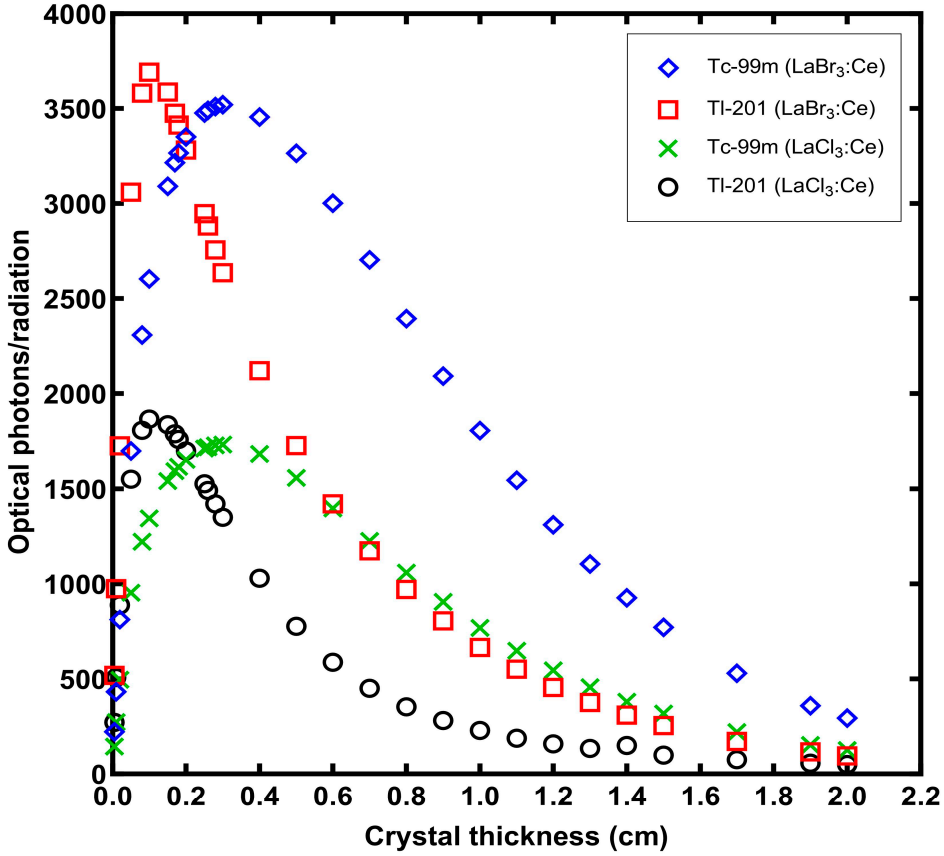

Figure 5. The predicted *DOG* values of $LaCl_3$:Ce and $LaBr_3$:Ce crystals for various thicknesses.

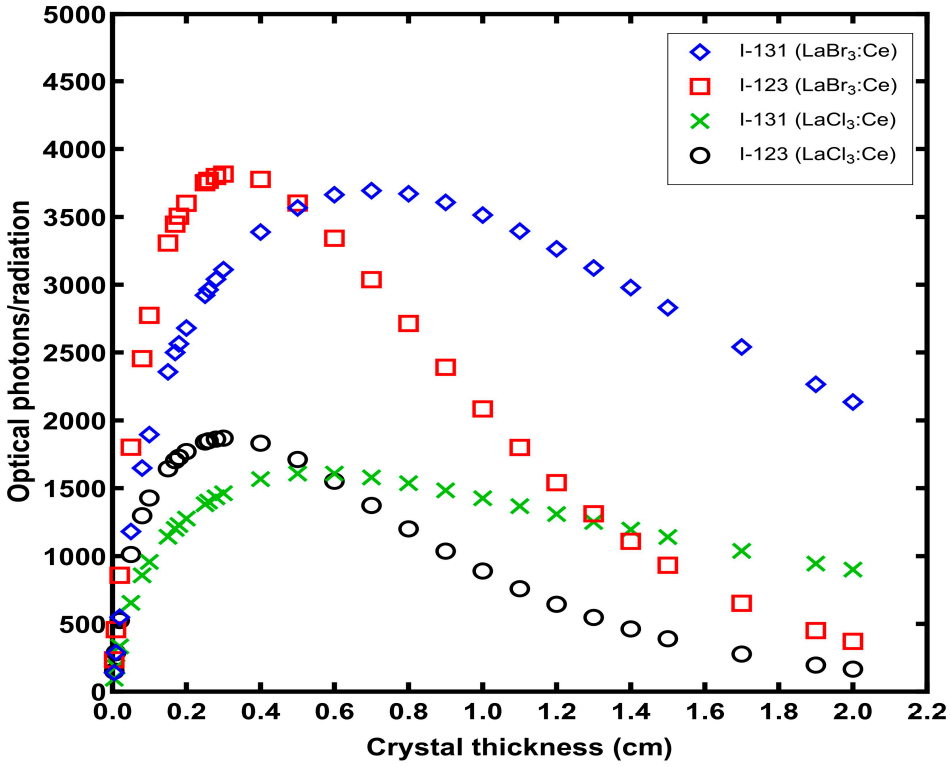

Figure 6. The predicted *DOG* values of $LaCl_3$:Ce and $LaBr_3$:Ce crystals for various thicknesses.

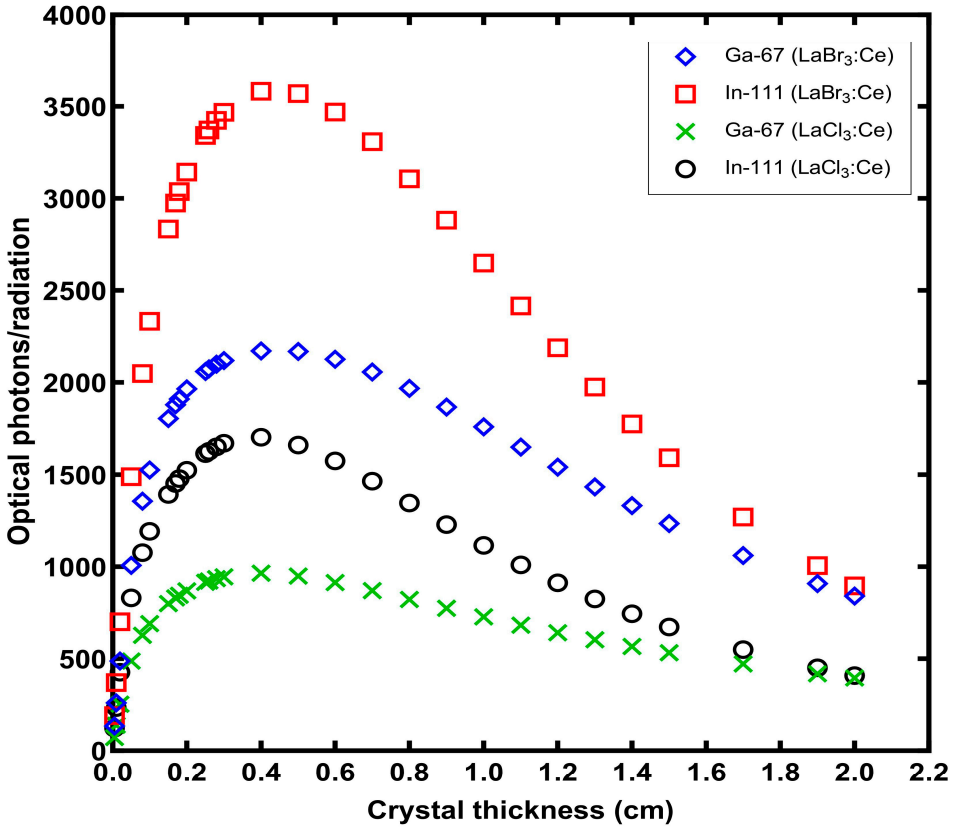

Figure 7. The predicted *DOG* values of $LaCl_3$:Ce and $LaBr_3$:Ce crystals for various thicknesses.

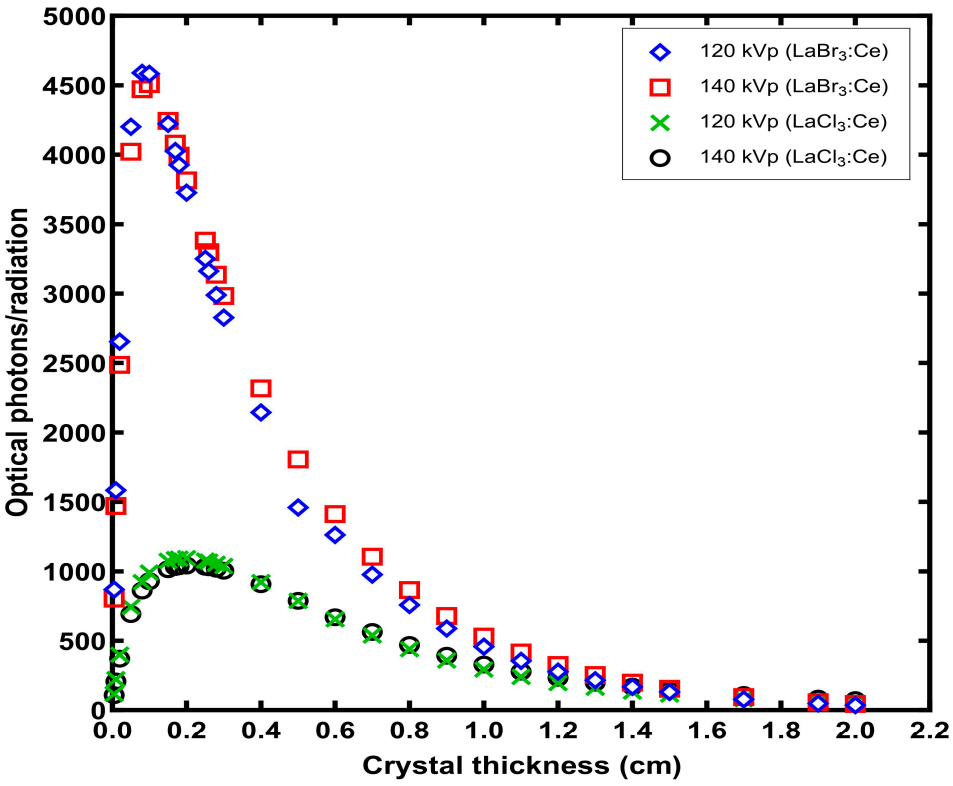

Figure 8. The predicted *DOG* values of $LaCl_3$:Ce and $LaBr_3$:Ce crystals for various thicknesses.

4. Discussion

The presented results are based on a theoretical analytical model which employs basic physical principles in ionizing radiation transfer and absorption. As such, it can provide a fast insight into the steps of radiation transfer, radiation absorption, optical photon production, and optical photon escape as a function of crystal thickness. The ionizing radiation interactions are treated assuming exponential attenuation of the radiation in the crystal while adopting the total attenuation coefficient as the radiation extinction parameter. The use of the total attenuation coefficient in low energies where the photoelectric absorption dominates provides accurate radiation absorption results. In the higher energies considered in this study, especially above 300 keV, the effect of scatter is of importance. The presented analytical method uses the attenuation coefficient as an extinction factor and may overestimate the radiation absorption since it assumes that all scatter photons and the characteristic radiation will be reabsorbed in the crystal. This may be valid for scatter photons of lower energy that might be subjected to photoelectric absorption, or for interactions in crystals with large dimensions. However, if small crystal thicknesses or secondary radiation generated close to the crystal surface are considered, then these photons possess a higher probability of escaping the crystal. Thus, analytical modeling overestimates the absorbed radiation energy. The extent of the overestimation depends upon the material, the interaction site, and the radiation energy. Subsequently, the optical photon propagation in the presented work is treated via an already published semi-empirical approach where the percentage of the optical photon transmission per layer is obtained by fitting experimental data, and the variation in the optical photon escape angles is not explicitly considered.

A more accurate prediction of the radiation and optical photons transfer and escape in the material, without a priori knowledge of the experimental *AE* results would require simulation tools, where an accurate geometry is necessary and the radiation and the optical transfer properties as well as the photon absorption lengths can be more accurately considered [42–48]. Despite a degree of overestimation in higher energies by the utilized analytical methodology and the corresponding assumption in the optical photon exit layer, the presented method can still provide useful qualitative results in terms of comparing the efficiency of different crystalline materials at different thicknesses when excited by ionizing radiation.

As observed in Figure 1, the average values of k for the $LaCl_3$:Ce and $LaBr_3$:Ce crystals are significantly higher compared to other single-crystal scintillators and comparable to those for CsI:Tl columnar phosphor [33,35,36]. Based on the assumptions of the model for the propagation of light within crystals, this difference is mainly attributed to the fact that all surfaces of the examined crystals, except the output surface, were covered with Teflon, thus minimizing losses by optical photon escape when the photons were incident on the crystal surfaces. As previously mentioned, according to the model, light losses, in addition to lateral light escape, can also occur due to internal optical photon absorption in the crystal mass. However, the absorption of the generated photons depends on the band gap width of the crystal in relation to the energy of the photons. In the case of $LaCl_3$:Ce, the energy of the majority of generated photons is 3.54 eV, whereas the estimated band gap of the crystal lies between 4.34 and 8.25 eV, with an intermediate value being more probable [49]. For $LaBr_3$:Ce, the photons have an energy of 3.26 eV, and the band gap is estimated to be between 3.42 and 7.43 eV [49]. Consequently, the reabsorption of the generated photons occurs in a very small percentage. In other words, both crystals are highly transparent to the visible radiation they produce.

The *DOG* values of the two crystals may be evidence that the $LaBr_3$:Ce crystal exhibits significantly better performance compared to the $LaCl_3$:Ce crystal, primarily due to its higher light yield [21,22]. The thickness of the crystal affects its optical performance in two ways. As the thickness increases, so does the absorption of incident X or gamma radiation and thus the production of optical photons. However, with increasing thickness, the losses of generated optical photons also exhibit a corresponding rise. Therefore, the optimal thickness is determined by the optimal combination of these two phenomena. For

low energies of incident radiation, where their absorption occurs at a shallow depth within the crystal, increasing the thickness of the crystal would decrease its optical performance, as it would increase the losses of optical photons without significantly contributing to their production. For higher energies of incident radiation, which are absorbed at greater depths, a thicker crystal is required, up to the point where the increased production of optical photons is not outweighed by their increased losses. Therefore, the optical performance of the crystal depends on the energy of the incident radiation, the thickness of the crystal, and the type of crystal.

It is worth commenting that the increased efficiency of $LaBr_3$:Ce in every case, compared to $LaCl_3$:Ce, is not only affected by the notable difference in the corresponding light yields (i.e., 63,000 photons/MeV for $LaBr_3$:Ce vs. 49,000 photons/MeV for $LaCl_3$:Ce). The total light output is also affected by the radiation energy absorbed and the probability of optical photon escape. For the same crystal thickness, the higher $LaBr_3$:Ce density (5.2 g/cm^3) with regard to that of $LaCl_3$:Ce (3.86 g/cm^3) enhances the probability of radiation interaction and subsequent energy absorption in $LaBr_3$:Ce with respect to $LaCl_3$:Ce. Consequently, a greater number of optical photons are produced in the $LaBr_3$:Ce scintillator when all the absorbed radiation is considered. Finally, the optical photon propagation probability per layer of $LaBr_3$:Ce is slightly higher than the corresponding $LaCl_3$:Ce as shown in Figure 1. Therefore, the higher probability of radiation absorption, the higher optical photon yield, and the more efficient optical photon propagation characteristics of $LaBr_3$:Ce combined result in the higher efficiency of $LaBr_3$:Ce with respect to $LaCl_3$:Ce.

Generally, it is evident that with the increase in energy, the optimum thickness increases for both crystals and reaches its maximum at the higher energy value of 511 keV in PET. As mentioned earlier, this was expected since the absorption of higher energy X or gamma photons occurs at a greater depth within the crystal. Thus, for PET applications, the optimal thickness for $LaCl_3$:Ce and $LaBr_3$:Ce crystals is 0.6 and 0.8 cm, respectively. For the energy range at which the radionuclides used in SPECT emit, the optimal thickness of $LaCl_3$:Ce and $LaBr_3$:Ce ranges from 0.1–0.5 cm and 0.1–0.7 cm, respectively, whereas for 120 and 140 KVp, the optimal thickness is 0.2 cm and 0.08–0.1 cm, respectively.

Approximately 80% of all nuclear medicine scans performed globally consist of SPECT and planar scintigraphy [50]. The most common clinical use of SPECT is in the assessment of myocardial perfusion and the evaluation of myocardial and coronary artery status following a cardiac ischemic episode [2,5]. The cardiological application of SPECT surpasses all other diagnostic applications of SPECT to such an extent that manufacturers offer SPECT systems that have been optimized for this type of imaging [5]. The most widely used isotope worldwide in this imaging technique, but not limited to it, is ^{99m}Tc [50,51]. For this isotope, it has been observed that the optimal thickness is 0.3 cm for both crystals. Another isotope that was initially used in cardiology nuclear imaging but continues to be utilized for certain advantages it offers, as well as in cases of ^{99m}Tc shortage, is ^{201}Tl [52], for which the optimal thickness of the two crystals is 0.1 cm.

^{123}I and ^{131}I are extensively used in nuclear imaging as well as in the radiation therapy of neuroendocrine tumors, such as thyroid cancer, comprising a theranostic pair [4,51,53,54]. ^{123}I, due to its shorter half-life and absence of beta particle emission, imposes a lower radiation burden on the subject compared to ^{131}I; therefore, it is more commonly used in nuclear imaging [4]. It is also particularly effective in visualizing serotonin and dopamine neurotransmitters, as well as in diagnosing neurodegenerative diseases, cerebrovascular disorders, and brain injuries [51]. From the results, for applications involving ^{123}I, the ideal crystal thickness for both crystals stands at 0.3 cm, whereas for ^{131}I, it stands at 0.5 cm and 0.7 cm for $LaCl_3$:Ce and $LaBr_3$:Ce, respectively.

^{67}Ga has been utilized for over fifty years in nuclear imaging, particularly for the diagnosis and localization of inflammatory areas within the body, such as in the case of pyrexia of unknown origin [53]. Furthermore, the scintigraphy with this isotope is used adjunctively for distinguishing between malignant and benign tumors, as well as in the evaluation of head and neck squamous cell carcinoma [55]. The optimal thickness for ^{67}Ga

was calculated as equal to 0.4 cm for both crystals. ^{111}In exhibits exceptional characteristics for nuclear imaging and is used for similar purposes as ^{67}Ga. ^{111}In is typically bound to antibodies, polypeptides, or white blood cells for the diagnosis and localization of inflammations within the body, for the diagnosis of cases with fever of unknown origin, or in cases where other diagnostic and imaging techniques yield ambiguous results [56,57]. Regarding uses related to ^{111}In, the ideal crystal thickness was found equal to 0.4 cm for both crystals.

In the field of nuclear medicine applications, the choice of the most suitable crystal scintillator thickness plays a pivotal role in optimizing patient care. An optimal crystal scintillator thickness allows for improved sensitivity in detecting gamma rays emitted by radiopharmaceuticals, which in turn translates to reduced required radioactivity administered to patients to achieve the desired diagnostic outcomes. This reduction translates to a substantial decrease in patient radiation exposure. Consequently, patients undergoing nuclear medicine procedures experience lower radiation exposure, which not only enhances their safety but also contributes to a more sustainable and patient-centric approach to nuclear medicine practice.

The presented theoretical *DOG* results demonstrate the applicability of different $LaBr_3$:Ce and $LaCl_3$:Ce crystal thicknesses with the radioisotopes currently in use in nuclear medicine applications and can be used as an initial reference for the development of crystals with different thicknesses. A more precise quantitative approach will require experimental *AE* results for each case.

5. Conclusions

In the current study, a theoretical model was developed to describe the light propagation within a crystal scintillator and to estimate the optimal thickness of $LaCl_3$:Ce and $LaBr_3$:Ce single-crystal scintillators in terms of Detector Optical Gain (*DOG*). Notably, the strong alignment between experimental observations and theoretical predictions of *AE* in both crystals underscores the reliability of the model. The values of k for $LaCl_3$:Ce and $LaBr_3$:Ce crystals are markedly superior in comparison to other single-crystal scintillators. Moreover, the discernibly superior *DOG* values of $LaBr_3$:Ce imply its enhanced performance compared to $LaCl_3$:Ce. Our observations also reveal that the optimal thickness depends on both the material of the scintillator and the energy of the gamma-rays and X-rays. These findings offer valuable insights into the design and optimization of crystal scintillators in the realm of Nuclear Medicine Imaging systems, providing a robust foundation for future advancements in this critical field.

Author Contributions: Conceptualization, S.T., C.M. and N.K.; methodology, S.T., C.M., I.V., G.F. and N.K.; software, S.T., N.K. and I.V.; validation, K.N., G.F. and I.K.; formal analysis, S.T., C.M., I.V. and A.B.; investigation, S.T., I.K., A.B. and K.N.; resources, C.M., I.V. and G.F.; data curation, I.V. and N.K.; writing—original draft preparation, S.T., C.M. and N.K.; writing—review and editing, S.T., C.M., I.K. and N.K.; visualization, C.M. and N.K.; supervision, N.K.; project administration, C.M. and N.K. All authors have read and agreed to the published version of the manuscript.

Funding: This research received no external funding.

Data Availability Statement: The data associated with our study are included or referenced in the article and can be made available on reasonable request.

Conflicts of Interest: The authors declare no conflicts of interest.

References

1. Cherry, S.R.; Sorenson, J.A.; Phelps, M.E. *Physics in Nuclear Medicine*, 4th ed.; Elsevier/Saunders: Philadelphia, PA, USA, 2012.
2. Lecomte, R.; Granja, C.; Leroy, C.; Stekl, I. Biomedical Imaging: SPECT and PET. *AIP Conf. Proc.* **2007**, *958*, 115–122. [CrossRef]
3. Eijk, C.W.E.V. Inorganic scintillators in medical imaging. *Phys. Med. Biol.* **2002**, *47*, 85–106. [CrossRef] [PubMed]
4. Morphis, M.; Van Staden, J.A.; du Raan, H.; Ljungberg, M. Evaluation of Iodine-123 and Iodine-131 SPECT activity quantification: A Monte Carlo study. *EJNMMI Phys.* **2021**, *8*, 61. [CrossRef] [PubMed]
5. Madsen, M.T. Recent Advances in SPECT Imaging. *J. Nucl. Med.* **2007**, *48*, 661–673. [CrossRef]

6. Zanzonico, P. Positron emission tomography: A review of basic principles, scanner design and performance, and current systems. *Semin. Nucl. Med.* **2004**, *34*, 87–111. [CrossRef]
7. Chowdhury, F.U.; Scarsbrook, A.F. The role of hybrid SPECT-CT in oncology: Current and emerging clinical applications. *Clin. Radiol.* **2008**, *63*, 241–251. [CrossRef] [PubMed]
8. Bailey, D.L. Transmission scanning in emission tomography. *Eur. J. Nucl. Med. Mol. Imaging* **1998**, *25*, 774–787. [CrossRef] [PubMed]
9. Cal-Gonzalez, J.; Rausch, I.; Shiyam Sundar, L.K.; Lassen, M.L.; Muzik, O.; Moser, E.; Papp, L.; Beyer, T. Hybrid Imaging: Instrumentation and Data Processing. *Front. Phys.* **2018**, *6*, 47. [CrossRef]
10. Beyer, T.; Freudenberg, L.S.; Townsend, D.W.; Czernin, J. The Future of Hybrid Imaging—Part 1: Hybrid Imaging Technologies and SPECT/CT. *Insights Imaging* **2011**, *2*, 161–169. [CrossRef]
11. Beyer, T.; Townsend, D.W.; Czernin, J.; Freudenberg, L.S. The Future of Hybrid Imaging—Part 2: PET/CT. *Insights Imaging* **2011**, *2*, 225–234. [CrossRef]
12. Guo, Z. The Principle and State-of-Art Facilities for PET. *J. Phys. Conf. Ser.* **2022**, *2386*, 012062. [CrossRef]
13. Marsden, P.K. Detector technology challenges for nuclear medicine and PET. *Nucl. Instrum. Methods Phys. Res. Sect. A Accel. Spectrometers Detect. Assoc. Equip.* **2003**, *513*, 1–7. [CrossRef]
14. Berard, P.; Pepin, C.M.; Rouleau, D.; Cadorette, J.; Lecomte, R. CT acquisition using PET detectors and electronics. *IEEE Trans. Nucl. Sci.* **2005**, *52*, 634–637. [CrossRef]
15. Van Loef, E.V.D.; Dorenbos, P.; Van Eijk, C.W.E.V.; Kramer, K.; Gudel, H.U. Scintillation properties of $LaCl_3$:Ce^{3+} crystals: Fast, efficient and high-energy-resolution scintillators. *IEEE Nucl. Sci. Symp. Conf. Rec.* **2000**, *6*, 31–34. [CrossRef]
16. Iltis, A.; Mayhugh, M.R.; Menge, P.; Rozsa, C.M.; Selles, O.; Solovyev, V. Lanthanum halide scintillators: Properties and applications. *Nucl. Instrum. Methods Phys. Res. Sect. A Accel. Spectrometers Detect. Assoc. Equip.* **2006**, *563*, 359–363. [CrossRef]
17. Van Loef, E.V.D.; Dorenbos, P.; Van Eijk, C.W.E.V.; Krämer, K.; Güdel, H.U. High-energy-resolution scintillator: Ce^{3+} activated $LaBr_3$. *Appl. Phys. Lett.* **2001**, *79*, 1573–1575. [CrossRef]
18. Van Loef, E.V.D.; Dorenbos, P.; Van Eijk, C.W.E.V.; Krämer, K.; Güdel, H.U. Scintillation properties of $LaBr_3$:Ce^{3+} crystals: Fast, efficient and high-energy-resolution scintillators. *Nucl. Instrum. Methods Phys. Res. Sect. A Accel. Spectrometers Detect. Assoc. Equip.* **2002**, *486*, 254–258. [CrossRef]
19. Advatech, U.K. LaCl3: Ce-Lanthanum Chloride (Ce). Available online: https://www.advatech-uk.co.uk/lacl3_ce.html (accessed on 12 May 2023).
20. Advatech, U.K. LaBr3: Ce-Lanthanum Bromide (Ce). Available online: https://www.advatech-uk.co.uk/labr3_ce.html (accessed on 12 May 2023).
21. Tseremoglou, S.; Michail, C.; Valais, I.; Ninos, K.; Bakas, A.; Kandarakis, I.; Fountos, G.; Kalyvas, N. Evaluation of Cerium-Doped Lanthanum Bromide ($LaBr_3$:Ce) Single-Crystal Scintillator's Luminescence Properties under X-ray Radiographic Conditions. *Appl. Sci.* **2022**, *13*, 419. [CrossRef]
22. Tseremoglou, S.; Michail, C.; Valais, I.; Ninos, K.; Bakas, A.; Kandarakis, I.; Fountos, G.; Kalyvas, N. Efficiency Properties of Cerium-Doped Lanthanum Chloride ($LaCl_3$:Ce) Single Crystal Scintillator under Radiographic X-ray Excitation. *Crystals* **2022**, *12*, 655. [CrossRef]
23. Bagheri, R.; Shirmardi, S.P.; Heidari, B.; Ahmadi, B.; Tuzemen, S. Comparison of $LaBr_3$(CE) and NaI(TL) Scintillation Crystals Responses to Various Gamma Energies Using Monte Carlo Simulations. *Int. J. Adv. Res.* **2016**, *4*, 494–500. [CrossRef]
24. Sharma, S.; Ranga, V.; Dhibar, M.; Rawat, S.; Kumar, G.A. Intrinsic Resolution of Compton Electrons in $LaBr_3$: Ce and $LaCl_3$: Ce Detectors Using Compton Coincidence Technique. *Nucl. Phys.* **2016**, *61*, 1020–1021.
25. Sariyal, R.; Mazumdar, I.; Patel, S.M. Measurement of Absolute Light Yield and Quantum Efficiency of $LaBr_3$: Ce Scintillator Detector Using SiPM. *J. Inst.* **2021**, *16*, P12024. [CrossRef]
26. Dey Chaudhuri, S.; Banerjee, D.; Bhattacharjee, T.; Wasim Raja, S.; Acharya, R.; Pujari, P.K. Performance Study of $LaBr_3$: Ce Detectors Coupled to R2083 PM Tube for Energy and Timing Characteristics. *J. Radioanal. Nucl. Chem.* **2020**, *324*, 829–835. [CrossRef]
27. Cazzaniga, C.; Nocente, M.; Tardocchi, M.; Fazzi, A.; Hjalmarsson, A.; Rigamonti, D.; Ericsson, G.; Gorini, G. Thin YAP:Ce and $LaBr_3$:Ce Scintillators as Proton Detectors of a Thin-Film Proton Recoil Neutron Spectrometer for Fusion and Spallation Sources Applications. *Nucl. Instrum. Methods Phys. Res. Sect. A Accel. Spectrometers Detect. Assoc. Equip.* **2014**, *751*, 19–22. [CrossRef]
28. Nácher, E.; Mårtensson, M.; Tengblad, O.; Álvarez-Pol, H.; Bendel, M.; Cortina-Gil, D.; Gernhäuser, R.; Le Bleis, T.; Maj, A.; Nilsson, T.; et al. Proton Response of CEPA4: A Novel $LaBr_3$(Ce)–$LaCl_3$(Ce) Phoswich Array for High-Energy Gamma and Proton Spectroscopy. *Nucl. Instrum. Methods Phys. Res. Sect. A Accel. Spectrometers Detect. Assoc. Equip.* **2015**, *769*, 105–111. [CrossRef]
29. Babiano, V.; Caballero, L.; Calvo, D.; Ladarescu, I.; Olleros, P.; Domingo-Pardo, C. γ -Ray Position Reconstruction in Large Monolithic $LaCl_3$(Ce) Crystals with SiPM Readout. *Nucl. Instrum. Methods Phys. Res. Sect. A Accel. Spectrometers Detect. Assoc. Equip.* **2019**, *931*, 1–22. [CrossRef]
30. Taggart, M.P.; Henderson, J. Fast-Neutron Response of $LaBr_3$(Ce) and $LaCl_3$(Ce) Scintillators. *Nucl. Instrum. Methods Phys. Res. Sect. A Accel. Spectrometers Detect. Assoc. Equip.* **2020**, *975*, 164201. [CrossRef]
31. Garnett, R.; Prestwich, W.V.; Atanackovic, J.; Wong, M.; Byun, S.H. Characterization of a $LaBr_3$(Ce) Detector for Gamma-Ray Spectrometry for CANDU Power Reactors. *Radiat. Meas.* **2017**, *106*, 628–631. [CrossRef]
32. Aldawood, S.; Castelhano, I.; Gernhäuser, R.; Van Der Kolff, H.; Lang, C.; Liprandi, S.; Lutter, R.; Maier, L.; Marinšek, T.; Schaart, D.R.; et al. Comparative Characterization Study of a $LaBr_3$(Ce) Scintillation Crystal in Two Surface Wrapping Scenarios: Absorptive and Reflective. *Front. Oncol.* **2015**, *5*, 270. [CrossRef]

33. Nikolopoulos, D.; Kalyvas, N.; Valais, I.; Argyriou, X.; Vlamakis, E.; Sevvos, T.; Kandarakis, I. A semi-empirical Monte Carlo based model of the Detector Optical Gain of Nuclear Imaging scintillators. *J. Inst.* **2012**, *7*, P11021. [CrossRef]
34. David, S.; Michail, C.; Seferis, I.; Valais, I.; Fountos, G.; Liaparinos, P.; Kandarakis, I.; Kalyvas, N. Evaluation of Gd_2O_2S: Pr granular phosphor properties for X-ray mammography imaging. *J. Lumin.* **2016**, *169*, 706–710. [CrossRef]
35. Kalyvas, N.; Valais, I.; Michail, C.; Fountos, G.; Kandarakis, I.; Cavouras, D. A theoretical study of CsI:Tl columnar scintillator image quality parameters by analytical modeling. *Nucl. Instrum. Methods Phys. Res. Sect. A Accel. Spectrometers Detect. Assoc. Equip.* **2015**, *779*, 18–24. [CrossRef]
36. Kalyvas, N.; Valais, I.; David, S.; Michail, C.; Fountos, G.; Liaparinos, P.; Kandarakis, I. Studying the energy dependence of intrinsic conversion efficiency of single crystal scintillators under X-ray excitation. *Opt. Spectrosc.* **2014**, *116*, 743–747. [CrossRef]
37. Roncali, E.; Stockhoff, M.; Cherry, S.R. An integrated model of scintillator-reflector properties for advanced simulations of optical transport. *Phys. Med. Biol.* **2017**, *62*, 4811–4830. [CrossRef] [PubMed]
38. Bernabei, R.; Belli, P.; Montecchia, F.; Nozzoli, F.; d'Angelo, A.; Cappella, F.; Incicchitti, A.; Prosperi, D.; Castellano, S.; Cerulli, R.; et al. Performances and potentialities of a $LaCl_3$:Ce scintillator. *Nucl. Instrum. Methods Phys. Res. Sect. A Accel. Spectrometers Detect. Assoc. Equip.* **2005**, *555*, 270–281. [CrossRef]
39. Giaz, A.; Pellegri, L.; Riboldi, S.; Camera, F.; Blasi, N.; Boiano, C.; Bracco, A.; Brambilla, S.; Ceruti, S.; Coelli, S.; et al. Characterization of large volume 3.5″×8″ $LaBr_3$:Ce detectors. *Nucl. Instrum. Methods Phys. Res. Sect. A Accel. Spectrometers Detect. Assoc. Equip.* **2013**, *729*, 910–921. [CrossRef]
40. RefractiveIndex. INFO. Available online: https://refractiveindex.info/ (accessed on 12 May 2023).
41. TASMIP Spectra Calculator. Available online: https://www.solutioinsilico.com/medical-physics/applications/tasmip-app.php?ans=0 (accessed on 14 March 2023).
42. Averyanov, D.; Blau, D. New Inogranic Scintillators' Application in the Electromagnetic Calorimetry in High-Energy Physics. *Appl. Sci.* **2023**, *13*, 6189. [CrossRef]
43. Nicolaidis, R.; Nozzoli, F.; Pepponi, G.; on behalf of the NUSES Collaboration. A Compact Particle Detector for Space-Based Applications: Development of a Low-Energy Module (LEM) for the NUSES Space Mission. *Instruments* **2023**, *7*, 40. [CrossRef]
44. Lakshminarayana, G.; Elmahroug, Y.; Kumar, A.; Tekin, H.O.; Rekik, N.; Dong, M.; Lee, D.-E.; Yoon, J.; Park, T. Detailed Inspection of γ-Ray, Fast and Thermal Neutrons Shielding Competence of Calcium Oxide or Strontium Oxide Comprising Bismuth Borate Glasses. *Materials* **2021**, *14*, 2265. [CrossRef]
45. Sarrut, D.; Bała, M.; Bardiès, M.; Bert, J.; Chauvin, M.; Chatzipapas, K.; Dupont, M.; Etxebeste, A.; M Fanchon, L.; Jan, S.; et al. Advanced Monte Carlo Simulations of Emission Tomography Imaging Systems with GATE. *Phys. Med. Biol.* **2021**, *66*, 10TR03. [CrossRef]
46. Sarrut, D.; Arbor, N.; Baudier, T.; Borys, D.; Etxebeste, A.; Fuchs, H.; Gajewski, J.; Grevillot, L.; Jan, S.; Kagadis, G.C.; et al. The OpenGATE Ecosystem for Monte Carlo Simulation in Medical Physics. *Phys. Med. Biol.* **2022**, *67*, 184001. [CrossRef]
47. Zhang, J.; Xiao, X.; Chen, Y.; Zhang, B.; Ma, X.; Ai, X.; Li, J. A Portable Three-Layer Compton Camera for Wide-Energy-Range Gamma-Ray Imaging: Design, Simulation and Preliminary Testing. *Sensors* **2023**, *23*, 8951. [CrossRef]
48. Zarrini-Monfared, Z.; Karbasi, S.; Zamani, A.; Mosleh-Shirazi, M.A. Full modulation transfer functions of thick parallel- and focused-element scintillator arrays obtained by a Monte Carlo optical transport model. *Med. Phys.* **2023**, *50*, 3651–3660. [CrossRef]
49. McIlwain, M.E.; Gao, D.; Thompson, N. First principle quantum description of the energetics associated with $LaBr_3$, $LaCl_3$, and Ce doped scintillators. In Proceedings of the 2007 IEEE Nuclear Science Symposium Conference Record, Honolulu, HI, USA, 26 October–3 November 2007; pp. 2460–2465. [CrossRef]
50. Crișan, G.; Moldovean-Cioroianu, N.S.; Timaru, D.G.; Andrieș, G.; Căinap, C.; Chiș, V. Radiopharmaceuticals for PET and SPECT Imaging: A Literature Review over the Last Decade. *Int. J. Mol. Sci.* **2022**, *23*, 5023. [CrossRef]
51. Pimlott, S.L.; Sutherland, A. Molecular tracers for the PET and SPECT imaging of disease. *Chem. Soc. Rev.* **2011**, *40*, 149–162. [CrossRef]
52. Pagnanelli, R.A.; Basso, D.A. Myocardial Perfusion Imaging with ^{201}Tl. *J. Nucl. Med. Technol.* **2010**, *38*, 1–3. [CrossRef]
53. Bailey, D.; Sabanathan, D.; Aslani, A.; Campbell, D.; Walsh, B.; Lengkeek, N. RetroSPECT: Gallium-67 as a Long-Lived Imaging Agent for Theranostics. *Asia Ocean. J. Nucl. Med. Biol.* **2021**, *9*, 1–8. [CrossRef]
54. Israel, O.; Pellet, O.; Biassoni, L.; De Palma, D.; Estrada-Lobato, E.; Gnanasegaran, G.; Kuwert, T.; la Fougere, C.; Mariani, G.; Massalha, S.; et al. Two decades of SPECT/CT—The coming of age of a technology: An updated review of literature evidence. *Eur. J. Nucl. Med. Mol. Imaging* **2019**, *46*, 1990–2012. [CrossRef]
55. Oohashi, M.; Toshima, H.; Hayama, K.; Ogura, I. Gallium-67 SPECT-CT for the evaluation of head and neck: Preliminary study on maximum standardised uptake value in lesions, and in the parotid and submandibular glands. *Pol. J. Radiol.* **2020**, *85*, 224–229. [CrossRef]
56. Lewis, S.S.; Cox, G.M.; Stout, J.E. Clinical Utility of Indium 111–Labeled White Blood Cell Scintigraphy for Evaluation of Suspected Infection. *Open Forum Infect. Dis.* **2014**, *1*, ofu089. [CrossRef]
57. Roca, M.; De Vries, E.F.J.; Jamar, F.; Israel, O.; Signore, A. Guidelines for the labelling of leucocytes with 111In-oxine. *Eur. J. Nucl. Med. Mol. Imaging* **2010**, *37*, 835–841. [CrossRef] [PubMed]